Chemical Science

ROYAL SOCIETY OF CHEMISTRY

EDGE ARTICLE

View Article Online
View Journal | View Issue

Cite this: *Chem. Sci.*, 2026, **17**, 6586

All publication charges for this article have been paid for by the Royal Society of Chemistry

From centrosymmetric $(C_4H_8N_5)(SbF_4)$ to polar $(C_4H_7N_4O)(SbF_4)$: a new UV nonlinear optical material achieved by functional group modulation

Zhi-Xiang Wang,[ac] Chun-Li Hu,[a] Chuan-Fu Sun, *[b] Jiang-Gao Mao [a] and Fang Kong *[ab]

Received 26th November 2025
Accepted 2nd February 2026

DOI: 10.1039/d5sc09256f

rsc.li/chemical-science

The design and synthesis of new ultraviolet nonlinear optical (NLO) materials is challenging due to the constraint relationship between their NLO efficiency and optical bandgap. Using a functional group modulation strategy, the π-conjugated organic cations and the distorted $[SbF_4]^-$ anions are assembled in both antiparallel and parallel arrangement modes, resulting in two new organic–inorganic hybrid fluoroantimonites, namely, centrosymmetric $(C_4H_8N_5)(SbF_4)$ and polar $(C_4H_7N_4O)(SbF_4)$. The polar $(C_4H_7N_4O)(SbF_4)$ demonstrates excellent comprehensive properties, including a strong SHG effect (4.2 × KDP), a wide bandgap (4.40 eV) and a short phase matchable wavelength (263 nm). This SHG intensity is the largest among the organic–inorganic hybrid perfluoroantimonites with an optical bandgap >4.20 eV. The SHG density calculation indicates that the NLO performance of $(C_4H_7N_4O)(SbF_4)$ mainly comes from the parallel-arranged organic groups, with their contribution accounting for 89.49%. This work proves that the arrangement of π-conjugated organic ligands can be modulated to a parallel mode by adjusting the number of hydrogen bond donors. Combined with a wide HOMO–LUMO gap, the functional group modulation method is an effective strategy for designing and synthesizing ultraviolet NLO materials.

Introduction

Ultraviolet nonlinear optical (UV NLO) materials play a significant role in modern science and technology due to their ability to extend the wavelength range of lasers to the ultraviolet region through the second harmonic generation (SHG) process. Broad applications can be found in optical sensors, quantum communication, biological imaging, *etc.*[1–7] It is well known that excellent UV nonlinear crystals should meet the following conditions: a broad bandgap, a strong SHG response, an appropriate birefringence, and excellent physicochemical stability.[2,8–13] However, due to the bandgap being inversely proportional to the SHG efficiency, it is very difficult to combine the above excellent properties in a single compound.

Fluoroantimonites have been regarded as a potential UV NLO material system,[14,15] because (i) Sb^{3+} ions with stereochemically active lone pairs usually can undergo second-order Jahn–Teller distortion, resulting in high anisotropy, (ii) the presence of fluorine elements causes a blue shift in the bandgap. Many inorganic fluoroantimonites have been reported as promising UV NLO materials, such as $Rb_2Sb(P_2O_7)F$ (5.1 × KDP, 4.76 eV) and $CsSbF_2SO_4$ (3.0 × KDP, 4.76 eV).[16,17] However, recent studies on UV NLO fluoroantimonites were mainly focused on metal sulfates and phosphates. Although these tetrahedral groups have a positive effect on the large bandgaps of the materials, the non-polar configuration limits the contribution of SHG intensity.[18–22] For such compounds an SHG response that is four times that of KDP is usually difficult to reach, such as $Rb_2SO_4{\cdot}(SbF_3)_2$ (0.5 × KDP, 4.69 eV), $NH_4SbF_2SO_4$ (0.7 × KDP, 4.67 eV), $K_2Sb(P_2O_7)F$ (4.0 × KDP, 4.74 eV), *etc.*[23–25] Thus, it is necessary to expand the types of functional groups beyond tetrahedra to enhance the SHG response of fluoroantimonites.

Recently, it has been found that compared with traditional inorganic π-conjugated units (BO_3^{3-}, $B_3O_6^{3-}$, *etc*), organic π-conjugated units not only possess greater hyperpolarizability and anisotropy[26–30] but also exhibit rich structural tunability (Fig. 1). If they can be introduced into fluoroantimonites, it is expected to break the current situation of generally low SHG intensity of UV transparent fluoroantimonites. Lately, Zhang and his coworkers reported a new oxyfluoroantimonite, namely, $(C_5H_5NO)(Sb_2OF_4)$, which can exhibit a large SHG response and a wide bandgap.[31] This work demonstrates the feasibility of exploring UV NLO materials in fluoroantimonites with organic π-conjugated groups. However, it is the only case breaking through 4 times that of KDP among the reported UV transparent

[a]*State Key Laboratory of Functional Crystals and Devices, Fujian Institute of Research on the Structure of Matter, Chinese Academy of Sciences, Fuzhou 350002, P. R. China. E-mail: kongfang@fjirsm.ac.cn*

[b]*State Key Laboratory of Structural Chemistry, Fujian Institute of Research on the Structure of Matter, Chinese Academy of Sciences, Fuzhou 350002, P. R. China. E-mail: cfsun@fjirsm.ac.cn*

[c]*College of Chemistry, Fuzhou University, Fuzhou 350108, P. R. China*

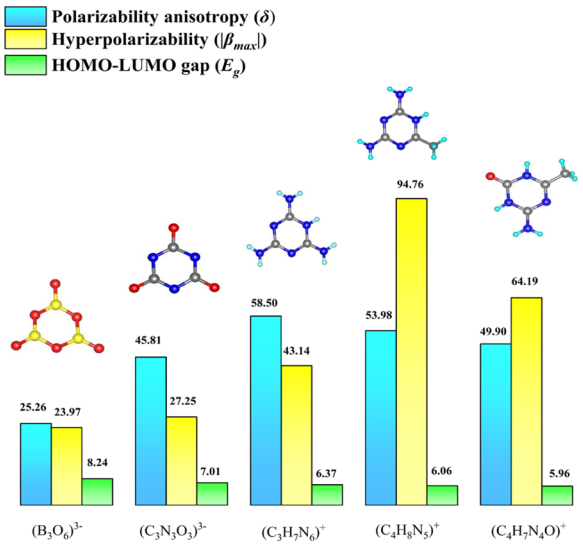

Fig. 1 The calculated values of polarizability anisotropy, hyperpolarizability and HOMO–LUMO gap for optically active groups.

organic–inorganic hybrid fluoroantimonites. Furthermore, noncentrosymmetric (NCS) fluoroantimonites with organic π-conjugated groups are also scarce, although such compounds contain two kinds of SHG functional units. The reason can be ascribed to the anti-parallel arrangement of the organic section, especially for those with large hyperpolarizability.

It is reported that hydrogen bonding can optimize the arrangement of organic units.[32–34] For example, by regulating the degree of intermolecular hydrogen bonds, compound TM1 crystallizes in the NCS space group ($P1$), showing a relatively large SHG response (3 × KDP), while compound TM2 crystallizes in the centrosymmetry (CS) space group ($P\bar{1}$) in an anti-parallel arrangement.[35] Inspired by these studies, our strategy is to modulate the type of functional group to change the number of the hydrogen bond donors (HBDs) and construct a new hydrogen bond network, with the aim of regulating the macroscopic symmetry of the structure (Fig. 2). After thorough screening, $(C_3H_7N_6)_2(SbF_5)\cdot H_2O$ with a melamine cation came into our focus.[36] On the one hand, melamine has enough amino functional groups, which can be replaced by non-HBDs, such as methyl and carbonyl groups. On the other hand, the modulated cations, such as $(C_4H_8N_5)^+$ and $(C_4H_7N_4O)^+$, can exhibit higher hyperpolarizability than that of $(C_3H_7N_6)^+$ while their HOMO–LUMO gaps still remain at a relatively high level (Fig. 1). It is expected to obtain a new UV NLO material through a functional group modulation strategy in organic–inorganic hybrid fluoroantimonites.

According to the above strategic guidance, two novel organic–inorganic hybrid fluoroantimonites, namely, $(C_4H_8N_5)(SbF_4)$ and $(C_4H_7N_4O)(SbF_4)$, have been successfully obtained by replacing the amino groups in melamine with methyl and carbonyl groups. With the decrease in hydrogen bonds between the organic cations, the structure undergoes a transformation from CS ($P\bar{1}$) to NCS (Pc). As expected, $(C_4H_7N_4O)(SbF_4)$ demonstrates an excellent comprehensive performance including a strong response (4.2 × KDP), a wide bandgap (4.40 eV), and a short UV cut-off edge (263 nm). It represents the second UV transparent organic–inorganic hybrid fluoroantimonite with SHG intensity higher than 4 × KDP. Herein, we report the syntheses, structures and optical properties of $(C_4H_8N_5)(SbF_4)$ and $(C_4H_7N_4O)(SbF_4)$.

Results and discussion

Since methyl groups are hydrophobic, if two of the hydrophilic amino groups on melamine molecules are replaced by methyl groups, it will reduce the solubility of the organic molecules in water, which is not conducive to crystal growth. So, the methoxy group with both hydrophilic and hydrophobic properties has been used to replace the amino group. It's worth noting that the methoxy group can undergo a demethylation reaction in an acidic environment to form a hydroxyl group, which then leads to enol isomerization and the formation of a ketone structure eventually[37,38] (Fig. 3). The demethylation of the methoxy group can be proved by the ^{1}H NMR spectrum (Fig. S1). No peak is observed at δ 3.60 ppm, which indicates that the methoxy group is no longer in the organic framework. A sharp single peak and a wide single peak appears at δ 2.10 ppm and 7.00 ppm, with the integral area corresponding to 3 hydrogen protons and 2 hydrogen protons, which can be respectively attributed to the proton signals of the methyl and amino groups.

Both $(C_4H_8N_5)(SbF_4)$ and $(C_4H_7N_4O)(SbF_4)$ single crystals were obtained by volatilizing aqueous solutions at room temperature (Fig. S2). Details of the synthesis procedure are outlined in the SI under the section titled "Syntheses". The purity of these crystals was verified using X-ray diffraction (XRD), as depicted in Fig. S3. Crystallographic details of $(C_4H_8N_5)(SbF_4)$ and $(C_4H_7N_4O)(SbF_4)$ can be found in Table S1.

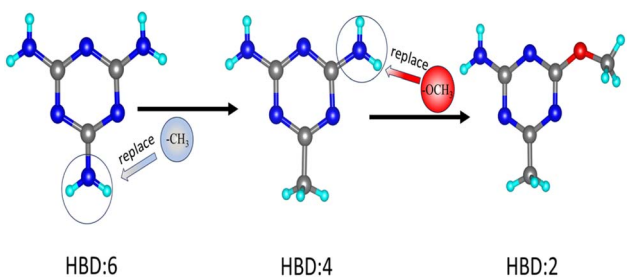

Fig. 2 The hydrogen bond donor (HBD) number decreases when the amino group has been replaced with methyl and methoxy groups.

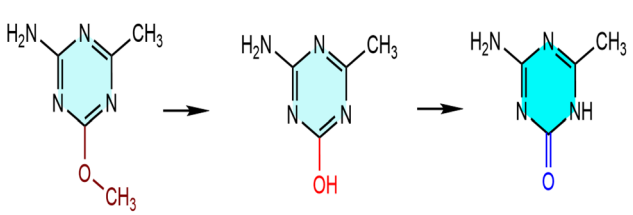

Fig. 3 The demethylation/enol isomerization step of $C_5H_8N_4O$.

Thermogravimetric (TG) tests show that $(C_4H_7N_4O)(SbF_4)$ is thermally stable at temperatures up to 105 °C and decomposes slowly when the temperature exceeds this value. $(C_4H_8N_5)(SbF_4)$ starts to decompose when the temperature exceeds 185 °C (Fig. S4). We believe that the significant difference in their thermal stability is mainly caused by the difference of hydrogen bond numbers in their unit cell.

$(C_4H_8N_5)(SbF_4)$ crystallizes in the triclinic system with the space group $P\bar{1}$ (no. 2), with the lattice parameters $a = 5.0998(3)$ Å, $b = 9.4607(5)$ Å, $c = 10.3378(6)$ Å, $\alpha = 68.330(5)°$, $\beta = 77.847(5)°$, $\gamma = 85.276(5)°$ and $V = 453.13(5)$ Å^3. There is one $(C_4H_8N_5)^+$ cation and one SbF_4^- anion in its asymmetric unit. Antimony is four-coordinated, producing a $[SbF_4]^-$ seesaw, with the bond length of Sb–F ranging from 1.9161(16) to 2.0646(16) Å. The bond-valence-sum results show that the bond valence is 3.046, indicating an oxidation state of +3. $(C_4H_8N_5)^+$ cations are connected to $[SbF_4]^-$ by N–H···F hydrogen bonding with the hydrogen bond length ranging from 1.757 to 2.056 Å (Fig. 4c). The adjacent $(C_4H_8N_5)^+$ cations are then connected by a *trans*-arrangement of N–H···N hydrogen bonds. The ordered arrangement of cations and anions interspersed along the *c*-axis forms the structure of $(C_4H_8N_5)(SbF_4)$ (Fig. 4d).

$(C_4H_7N_4O)(SbF_4)$ crystallizes in the monoclinic space group *Pc* (no. 7). The lattice parameters are $a = 11.4719(5)$ Å, $b = 4.6982(2)$ Å, $c = 9.1703(4)$ Å, $\alpha = \gamma = 90°$, $\beta = 113.104(5)°$ and $V = 454.61(4)$ Å^3. Its asymmetric unit contains one SbF_4^- anion and one $(C_4H_7N_4O)^+$ cation. The Sb–F distance is in the range of 1.927(3) to 2.068(3) Å. The bond-valence-sum results show that the bond valence is 2.987, suggesting that the oxidation state is +3 (Table S2). $C_4H_7N_4O^+$ cations are connected to $[SbF_4]^-$ *via* N–H···F hydrogen bonding (Fig. 4f) with the hydrogen bond length ranging from 1.820 to 1.946 Å. Each SbF_4^- anion is fixed by three $(C_4H_7N_4O)^+$ cations and arranged along the *c*-axis, forming a new three-dimensional network. The dipole moment of the $[SbF_4]$ seesaw in $(C_4H_7N_4O)(SbF_4)$ was calculated. Its local dipole moment is 9.18–9.98 D and the net dipole moment for a unit cell is 16.40 D, which implies its polar nature.

From $(C_3N_6H_7)_2(SbF_5)\cdot H_2O$ to $(C_4H_8N_5)(SbF_4)$ and then to $(C_4H_7N_4O)(SbF_4)$, the crystal structure realizes the transformation from a CS to a NCS structure. To better illustrate this transition, we make a detailed comparison of the three crystals. We can see that in their basic structural unit, the anions do not change much except from $[SbF_5]^{2-}$ to $[SbF_4]^-$, and the difference is mainly in the arrangement of cations. As shown in Table S3, the bond lengths and bond angles of the N–H···F hydrogen bonds in these three crystals change very little, but in $(C_4H_7N_4O)(SbF_4)$, the numbers of both N–H···F and N–H···N hydrogen bonds have decreased. Due to the large number of hydrogen bond donors ($-NH_2$ and $-NH^+$), it can be seen that in $(C_3N_6H_7)_2(SbF_5)\cdot H_2O$ and $(C_4H_8N_5)(SbF_4)$, even though a methyl group has been replaced by an amino group, organic cations can still be connected by N–H···N hydrogen bonds, forming a *trans*-arrangement (Fig. 4a and c), which is not favourable for the formation of NCS structures. However, in $(C_4H_7N_4O)(SbF_4)$, after undergoing enol tautomerism, another amino group in the organic molecule is substituted by an oxygen atom. The number of hydrogen bond donors is reduced, and the four strong electronegative F atoms in the anions are sufficient to anchor them all, which causes the connection between the organic cations to be shielded, breaking the original *trans*-arrangement (Fig. 4e).

The UV-vis-NIR diffuse reflectance spectra (Fig. 5a and b) show that the UV cutoff edges of $(C_4H_8N_5)(SbF_4)$ and $(C_4H_7N_4O)(SbF_4)$ are 261 nm and 263 nm, respectively, corresponding to experimental bandgaps of 4.42 eV and 4.40 eV. In addition, it is worth noting that the UV cutoff edge of the template $(C_3N_6H_7)_2(SbF_5)\cdot H_2O$ is 261 nm with an experimental bandgap of 4.74 eV, which can indicate that our modification of the organic groups has almost no effect on the UV cutoff edge, and this is conducive to the design of new UV transmittable crystals.

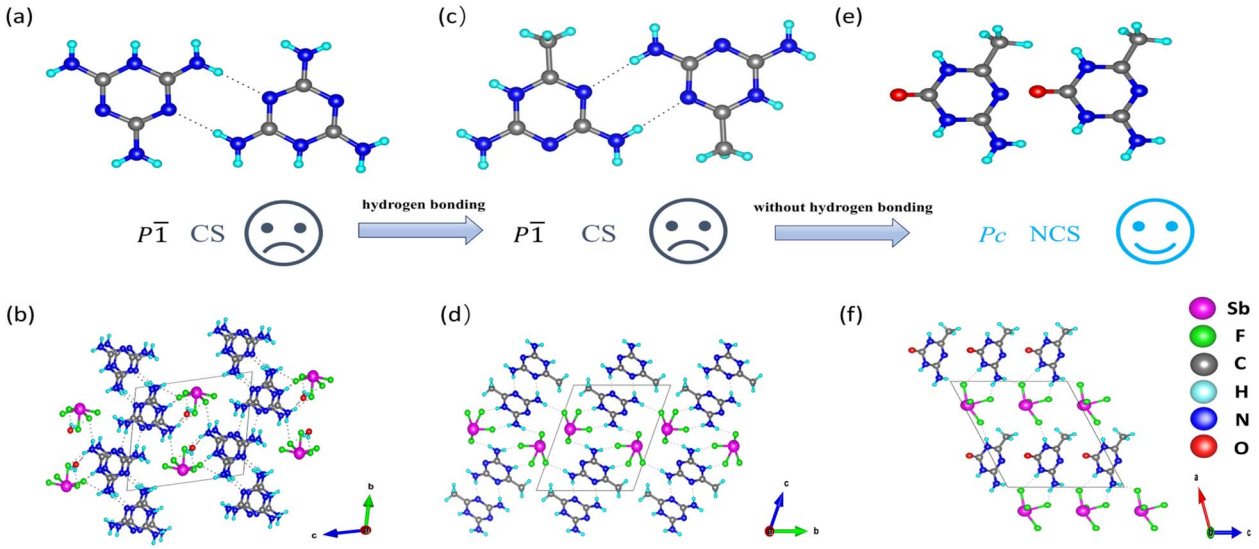

Fig. 4 The arrangement patterns of $(C_3N_6H_7)^+$ (a), $(C_4H_8N_5)^+$ (c) and $(C_4H_7N_4O)^+$ (e). The crystal structures of $(C_3N_6H_7)_2(SbF_5)\cdot H_2O$ (b), $(C_4H_8N_5)(SbF_4)$ (d) and $(C_4H_7N_4O)(SbF_4)$ (f).

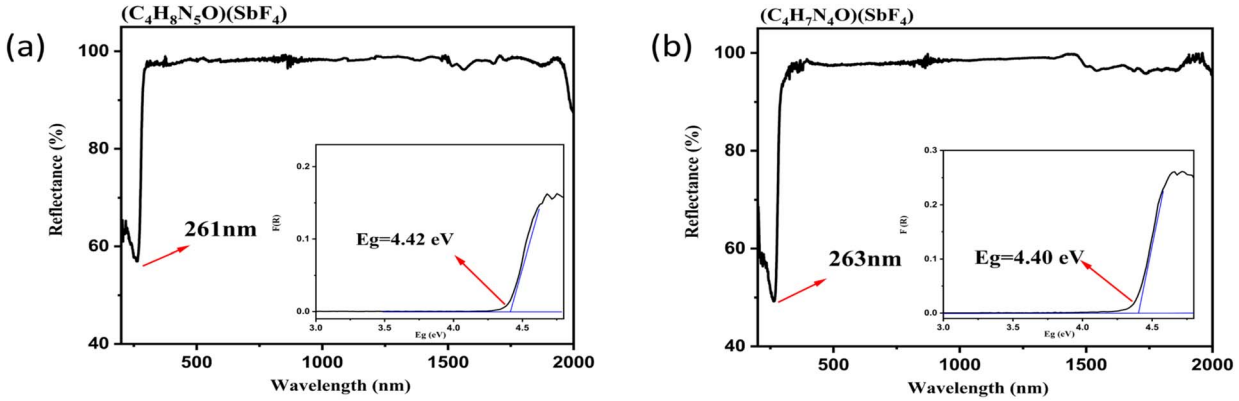

Fig. 5 The experimental bandgaps of $(C_4H_8N_5)(SbF_4)$ (a) and $(C_4H_7N_4O)(SbF_4)$ (b).

Based on the Kurtz–Perry method,[39–42] the powder SHG measurement of $(C_4H_7N_4O)(SbF_4)$ was accomplished under 1064 nm laser irradiation, and standard KH_2PO_4 (KDP) crystals were used as a reference. As shown in Fig. 6a, $(C_4H_7N_4O)(SbF_4)$ displays a strong SHG effect of 4.2 × KDP. Meanwhile, as the particle size increases, the intensity of SHG also increases, which indicates that it has phase matching (PM) capability (Fig. 6b). To evaluate the excellent properties of $(C_4H_7N_4O)(SbF_4)$, we further compared it with some reported UV inorganic antimonates and UV organic–inorganic hybrid fluoroantimonates (Table S4) such as $NaSbF_4$ (3.2 × KDP), $(NH_4)SbCl_2(SO_4)$ (1.7 × KDP), $CsSbF_2SO_4$ (3 × KDP), and $Rb_2SO_4\cdot(SbF_3)_2$ (2.2 × KDP) and $C(NH_2)_3SbF_4$ (2.0 × KDP), $SbF_3\cdot Gly$ (3.6 × KDP), $(C_5H_7N_2)Sb_2F_7$ (2.0 × KDP), and α-$2SbF_3\cdot Gly$ (3.3 × KDP).[17,23,31,43–47] Among organic–inorganic hybrid antimony-based UV NLO materials, its SHG response is only lower than that of $(C_5H_5NO)(Sb_2OF_4)$. So, $(C_4H_7N_4O)(SbF_4)$ possesses the largest SHG intensity in organic–inorganic hybrid perfluoroantimonites with a bandgap >4.20 eV (Fig. 6c). The r-on-1 test scheme was used to detect the powder LIDT of $(C_4H_7N_4O)(SbF_4)$ and $AgGaS_2$, yielding values of 65 and 4 MW cm^{-2}, indicating that the LIDT of $(C_4H_7N_4O)(SbF_4)$ is about 16 times that of $AgGaS_2$.

It is known that appropriate birefringence is essential for efficient phase matching during the SHG process. High birefringence exacerbates walk-off issues, while low birefringence makes phase matching challenging to achieve.[48–50] Thus, the birefringence was analyzed (Fig. 7). Fig. 7a shows the calculated

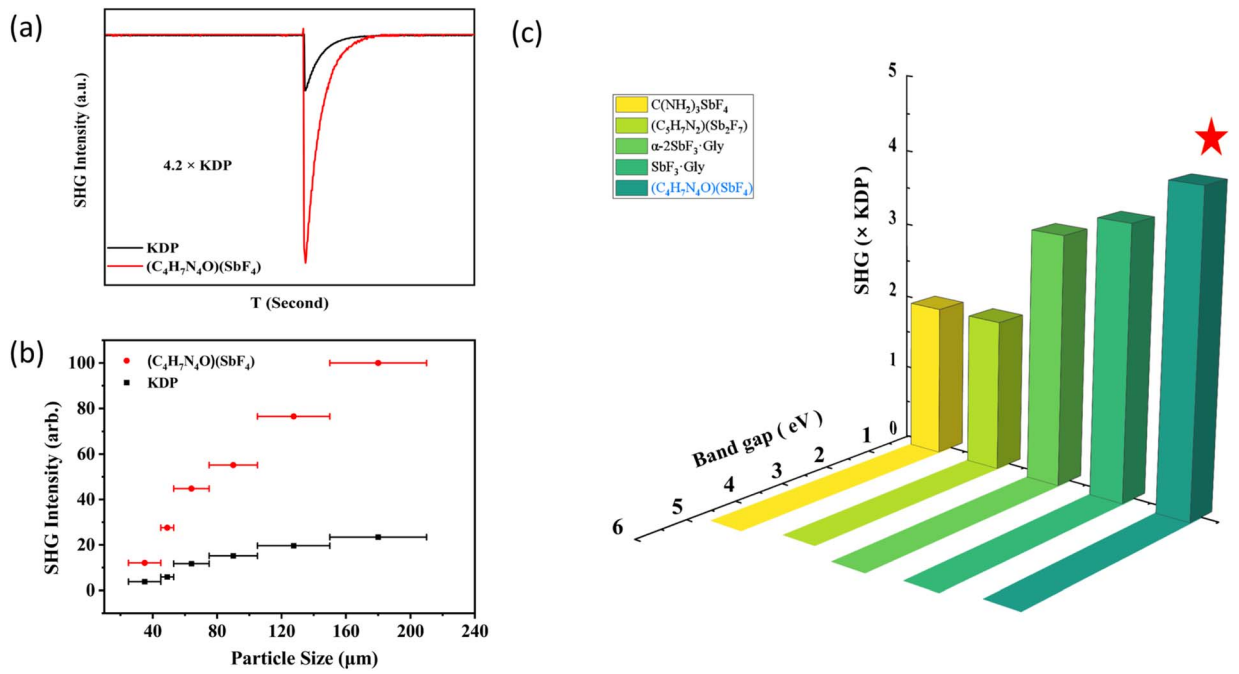

Fig. 6 Oscilloscope trace of the SHG signals for $(C_4H_7N_4O)(SbF_4)$ (150–210 μm) (a) and the relationship between the SHG intensity and the particle size of $(C_4H_7N_4O)(SbF_4)$ under 1064 nm laser irradiation (b). Comparison of the SHG efficiencies and optical bandgaps (>4.20 eV) among reported organic–inorganic hybrid perfluoroantimonites (fluorooxoantimonites were not included) (c).

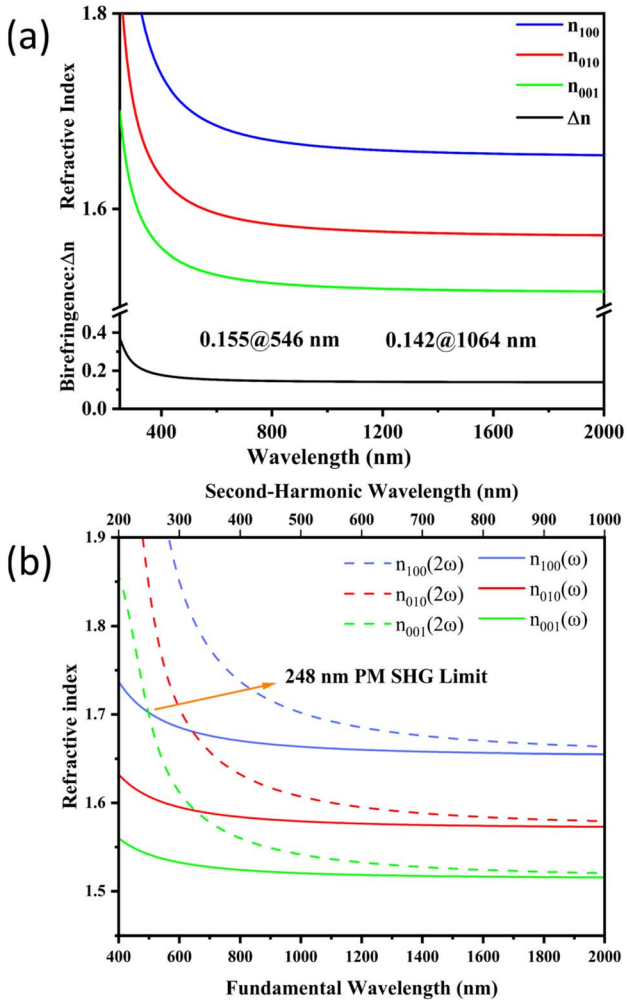

Fig. 7 The calculated birefringence curves of $(C_4H_7N_4O)(SbF_4)$ (a) and the calculated shortest phase matching wavelength of $(C_4H_7N_4O)(SbF_4)$ (b) based on the calculated refractive indices.

birefringence curves of $(C_4H_7N_4O)(SbF_4)$ and its birefringence was calculated to be 0.155 at 546 nm, which falls between that of $(C_3N_6H_7)_2(SbF_5)\cdot H_2O$ (0.380@550 nm) and $(C_4H_8N_5)(SbF_4)$ (0.059@546 nm) (Fig. S5). From Fig. 7b we can find that the shortest phase matching wavelength of $(C_4H_7N_4O)(SbF_4)$ reaches 248 nm. However, because its UV cut off edge was measured to be 263 nm (Fig. 5b), so its phase matching limit should be 263 nm and $(C_4H_7N_4O)(SbF_4)$ is a full-wavelength phase matching compound.

The infrared (IR) spectra of $(C_4H_8N_5)(SbF_4)$ and $(C_4H_7N_4O)(SbF_4)$ were analyzed in the wavelength range of 4000–400 cm^{-1} at room temperature. Fig. S6 shows the IR spectra of the compounds. The peaks at 3375 and 3183 cm^{-1} correspond to N–H vibrations. The absorption peaks observed at 2932–2769 cm^{-1} and 1032–722 cm^{-1} can be attributed to C–H vibrations. Sharp peaks between 1760 and 1600 cm^{-1} are associated with C=O vibration. The peaks around 1535–1308 cm^{-1} and 1082 cm^{-1} are assigned to $-CH_3$ bending and C–N vibrations, respectively. In addition, the peaks of Sb–F vibrations can be observed at 600–450 cm^{-1} (Table S5). The above

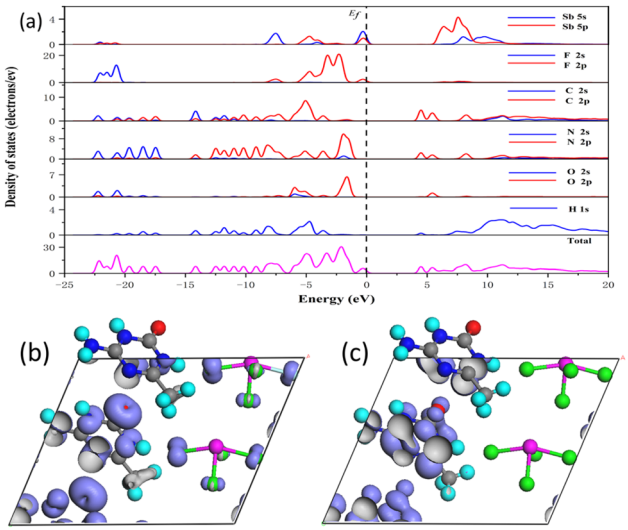

Fig. 8 The total and partial density of states (a) and SHG density of d_{11} in the VB (b) and the CB (c) for $(C_4H_7N_4O)(SbF_4)$.

attributions are consistent with the reports of the previous compounds.[51]

To further understand the structure–property relationship of $(C_4H_8N_5)(SbF_4)$ and $(C_4H_7N_4O)(SbF_4)$, theoretical calculation was performed using density functional theory (DFT).[52] The calculation results along the high-symmetry points of the first Brillouin zone show that $(C_4H_8N_5)(SbF_4)$ and $(C_4H_7N_4O)(SbF_4)$ are indirect band gap compounds with theoretical bandgaps of 3.23 eV and 2.89 eV (Fig. S7), respectively. Both experimental bandgaps are larger than the calculated values, which might be due to the limitation of the generalized gradient approximation method. Therefore, in an effort to analyse the optical properties of $(C_4H_8N_5)(SbF_4)$ and $(C_4H_7N_4O)(SbF_4)$ accurately, the scissor operator with 1.19 eV and 1.51 eV was utilized.

The partial and total density of states (DOS) of $(C_4H_8N_5)(SbF_4)$ and $(C_4H_7N_4O)(SbF_4)$ are shown in Fig. 8a and S8. For $(C_4H_8N_5)(SbF_4)$, the top of the valence band (VB) is mainly occupied by Sb-5s5p and F-2p, whereas the bottom of the conduction band (CB) is primarily contributed by N-2p and C-2p, indicating that the bandgap of $(C_4H_8N_5)(SbF_4)$ is dominated by Sb, F, N and C atoms. The VB near the Fermi level of $(C_4H_7N_4O)(SbF_4)$ is predominately composed of Sb-5s5p and F-2p, while the CB bottom is mainly consisted of N-2p and C-2p. It indicates that the bandgap of $(C_4H_7N_4O)(SbF_4)$ is primarily determined by Sb, F, N and C atoms. According to the SHG density data, its NLO performance mainly comes from organic assembly (Fig. 8b and c), with its contribution accounting for as high as 89.49%. Although the inorganic $[SbF_4]$ unit contributes little (10.50%) to the SHG effect, it is crucial for the formation of the NCS structure due to its polar nature.

Conclusions

In conclusion, we have created an NCS organic–inorganic hybrid fluoroantimonite with excellent SHG performance by adopting a functional group modulation strategy. The inorganic

part was focused on the $[SbF_4]^-$ group while the organic part was changed from $(C_4H_8N_5)^+$ to $(C_4H_7N_4O)^+$. When the HBD number was decreased from 5 to 4, the arrangement of the organic units was changed from anti-parallel mode to parallel mode. The polarity of organic and inorganic groups has been combined mutually, resulting in the polar structure of $(C_4H_7N_4O)(SbF_4)$. As we expected, $(C_4H_7N_4O)(SbF_4)$ features a strong SHG intensity of about 4.2 × KDP, a wide bandgap of 4.40 eV and a short PM wavelength of 263 nm. Compared with the reported work, the SHG intensity of $(C_4H_7N_4O)(SbF_4)$ is the largest among the organic–inorganic hybrid perfluoroantimonites with an optical bandgap >4.20 eV. Our work not only provides a promising candidate for UV NLO materials but also offers an effective strategy for novel SHG materials design.

Author contributions

Zhi-Xiang Wang: investigation, formal analysis, experimental manipulation, writing – original draft. Chun-Li Hu: theoretical calculations. Chuan-Fu Sun: resources, formal analysis, writing – review & editing. Jiang-Gao Mao: supervision, resources, funding acquisition. Fang Kong: conceptualization, project administration, writing – review & editing. All authors have given approval to the final version of the manuscript.

Conflicts of interest

There are no conflicts to declare.

Data availability

The data that support the findings of this study are available in the supplementary information (SI) of this article. Supplementary information: experimental section, computational method, crystal data, important bond distances and bond valences, elemental analysis, PXRD patterns, TGA curves, IR spectra, UV-visible-NIR diffuse reflectance spectra and band structures. See DOI: https://doi.org/10.1039/d5sc09256f.

CCDC 2474438 and 2474439 contain the supplementary crystallographic data for this paper.[53a,b]

Acknowledgements

This work was supported by the National Natural Science Foundation of China (Grant No. 22475215 and 22375201), the Natural Science Foundation of Fujian Province (Grant No. 2024J010039 and 2023j01216) and the Self-deployed Key Project of State Key Laboratory of Functional Crystals and Devices (GNJT-2025-ZD01).

References

1 D. Dou, C. Wei, B. Zhang, D. Yang and Y. Wang, *Angew. Chem., Int. Ed.*, 2025, **64**, e202504761.
2 F. Gong, X. Jiang, K. Duanmu, C. Wu, Z. Lin, Z. Huang, M. G. Humphrey and C. Zhang, *Angew. Chem., Int. Ed.*, 2025, e21786.
3 C. Jin, Y. Li, J. S. Kim, J. H. Lim, H. Huang, C. A. Chen, J. Lee, Y. Heo, B. Zhang, J. I. Jang and K. M. Ok, *Angew. Chem., Int. Ed.*, 2025, **64**, e202512618.
4 P. F. Li, C. L. Hu, J. G. Mao and F. Kong, *Coord. Chem. Rev.*, 2024, **517**, 216000.
5 X. Long, F. Li, H. Qiu, X. Hou, J. Lu, J. Li, Z. Yang, J. Cao, S. Pan and M. Mutailipu, *Angew. Chem., Int. Ed.*, 2025, e22210.
6 H. Qiu, S. Pan and M. Mutailipu, *Fundam. Res.*, 2025, **5**, 640–653.
7 H. Tian, C. Lin, Y. Zhou, X. Zhao, H. Fan, T. Yan, N. Ye and M. Luo, *Angew. Chem., Int. Ed.*, 2023, **62**, e202304858.
8 Z. Chen, C. Li, X. Wu, J. Lu, Z. Yang, X. Hou and M. Mutailipu, *Aggregate*, 2025, **6**, e70134.
9 T. T. He, F. Kong and J. G. Mao, *J. Synth. Cryst.*, 2025, **54**(10), 1811–1822.
10 H. Liu, X. Zhai, X. Li, H. Wu, Z. Hu, J. Wang, Y. Wu and H. Yu, *Angew. Chem., Int. Ed.*, 2025, **64**, e202502252.
11 J. Lu, X. Liu, M. Zhao, X. B. Deng, K. X. Shi, Q.-R. Wu, L. Chen and L.-M. Wu, *J. Am. Chem. Soc.*, 2021, **143**, 3647–3654.
12 X. Wen, Y. Yan, J. Lu, X. Shi, P. Tang, J. Chen, G. Yang, G. Peng, H. Yu, H. Zhang, Z. Hu, J. Wang and N. Ye, *Angew. Chem., Int. Ed.*, 2025, **64**, e202424153.
13 M. Yan, C.-L. Hu, R.-L. Tang, W. D. Yao, W. Liu and S.-P. Guo, *Chem. Sci.*, 2024, **15**, 8500–8505.
14 X. Dong, L. Huang, H. Zeng, Z. Lin, K. M. Ok and G. Zou, *Angew. Chem., Int. Ed.*, 2025, **64**, e202509917.
15 J. H. Wu, B. Zhang, T.-K. Jiang, F. Kong and J. G. Mao, *Chin. J. Struct. Chem.*, 2023, **42**, 100016.
16 X. Dong, H. Huang, L. Huang, Y. Zhou, B. Zhang, H. Zeng, Z. Lin and G. Zou, *Angew. Chem., Int. Ed.*, 2024, **63**, e202318976.
17 X. Dong, L. Huang, C. Hu, H. Zeng, Z. Lin, X. Wang, K. M. Ok and G. Zou, *Angew. Chem., Int. Ed.*, 2019, **58**, 6528–6534.
18 X. Chen, Y. Li, J. Luo and S. Zhao, *Chin. J. Struct. Chem.*, 2023, **42**, 100044.
19 P. F. Li, C. L. Hu, Y. F. Li, J. G. Mao and F. Kong, *J. Am. Chem. Soc.*, 2024, **146**, 7868–7874.
20 Y. Li, F. Liang, S. Zhao, L. Li, Z. Wu, Q. Ding, S. Liu, Z. Lin, M. Hong and J. Luo, *J. Am. Chem. Soc.*, 2019, **141**, 3833–3837.
21 H. Liu, H. Wu, Z. Hu, J. Wang, Y. Wu, P. S. Halasyamani and H. Yu, *ACS Mater. Lett.*, 2022, **5**, 155–161.
22 X. Zhang, B. Xu, D. Xiao, X. Zhang, P. Gong and Z. Lin, *Inorg. Chem. Front.*, 2025, **12**, 7566–7572.
23 Q. Wang, L. Wang, X. Zhao, L. Huang, D. Gao, J. Bi, X. Wang and G. Zou, *Inorg. Chem. Front.*, 2019, **6**, 3125–3132.
24 F. He, Y. Ge, X. Zhao, J. He, L. Huang, D. Gao, J. Bi, X. Wang and G. Zou, *Dalton Trans.*, 2020, **49**, 5276–5282.
25 S. V. Krivovichev and L. Bindi, *Angew. Chem., Int. Ed.*, 2020, **60**, 3854–3855.
26 R. N. Li, Z. C. Wu, W. D. Yao, Y. F. Fu, Y. M. Zhang, W. Liu, J. Wu and S. P. Guo, *Adv. Funct. Mater.*, 2025, e25860.
27 R. Wei, H. Huang, D. Yang, Y. Wang and B. Zhang, *Adv. Opt. Mater.*, 2024, **12**, 2401814.
28 J. Wu, Y. Guo, J. L. Qi, W. D. Yao, S. X. Yu, W. Liu and S. P. Guo, *Angew. Chem., Int. Ed.*, 2023, **62**, e202301937.

29 J. H. Wu, C. L. Hu, Y. F. Li, J. G. Mao and F. Kong, *Chem. Sci.*, 2024, **15**, 8071–8079.
30 Z. P. Zhang, X. Liu, R. X. Wang, S. Zhao, W. J. He, H. Y. Chen, X. B. Deng, L. M. Wu, Z. Zhou and L. Chen, *Angew. Chem., Int. Ed.*, 2024, **63**, e202408551.
31 L. Qi, X. Jiang, K. Duanmu, C. Wu, Z. Lin, Z. Huang, M. G. Humphrey and C. Zhang, *J. Am. Chem. Soc.*, 2024, **146**, 9975–9983.
32 D. Yang, H. Sha, Z. Wang, R. Su, C. He, B. Su, X. Yang and X. Long, *Adv. Opt. Mater.*, 2024, **12**, 2401762.
33 L. Yang, H. Mi, Q. Li, D. Yang, H. Sha, Z. Wang, R. Su, B. Su and C. He, *Mater. Today Chem.*, 2025, **48**, 102931.
34 Y. Wu, Y. Li, Y. Zhang, B. Teng, X. Jiang, C. Hu, S. Sun, L. Cao, J. Ma, K. Xu, D. Xu, Z. Lin and D. Zhong, *Adv. Funct. Mater.*, 2025, **35**, 2503125.
35 R. Zhao, T. Zhu, S. Wang, C. Jarrett-Wilkins, A. M. Najjarian, A. J. Lough, S. Hoogland, E. H. Sargent and D. S. Seferos, *Chem. Sci.*, 2022, **13**, 12144–12148.
36 Y. Shen, B. Chen, H. Chen and J. Luo, *Inorg. Chem.*, 2022, **61**, 14242–14246.
37 M. Bocus, E. Van Den Broeck, X. Wu, M. Bal, J. Bomon, L. Vanduyfhuys, B. F. Sels, B. U. W. Maes and V. Van Speybroeck, *Nat. Catal.*, 2025, **8**, 33–45.
38 Y. Lyu, M. Peng, Y. Hu, X. Hu, Y. Zhang, P. Zhao, T. Wang, S. Xu, K. Zhang and L. Bian, *Cell. Biomater.*, 2025, **1**, 100124.
39 D. Chu, K. Zhang, C. Xie, K. T. Butler, Z. Yang and S. Pan, *ACS Mater. Lett.*, 2024, **6**, 1094–1102.
40 Y. Kang, C. Yang, J. Zhang and Q. Wu, *Chin. Chem. Lett.*, 2026, **37**, 111385.
41 H. Yu, N. Z. Koocher, J. M. Rondinelli and P. S. Halasyamani, *Angew. Chem., Int. Ed.*, 2018, **57**, 6100–6103.
42 X. Zhang, J. Q. Shen, H. X. Lv, P. H. Guo, Y. G. Chen, C. L. Hu and X. M. Zhang, *Inorg. Chem. Front.*, 2025, **12**, 5430–5438.
43 G. Zhang, J. Qin, T. Liu, Y. Li, Y. Wu and C. Chen, *Appl. Phys. Lett.*, 2009, **95**, 261104.
44 F. He, Q. Wang, C. Hu, W. He, X. Luo, L. Huang, D. Gao, J. Bi, X. Wang and G. Zou, *Cryst. Growth Des.*, 2018, **18**, 6239–6247.
45 M. Zhang, B. Zhang, D. Yang and Y. Wang, *Inorg. Chem.*, 2021, **60**, 18483–18489.
46 Z. Bai, J. Lee, C. L. Hu, G. Zou and K. M. Ok, *Chem. Sci.*, 2024, **15**, 6572–6576.
47 Y. Kuk, Z. Bai, Y. Li and K. M. Ok, *Chem. Mater.*, 2025, **37**, 1306–1313.
48 P. F. Li, C. L. Hu, B. Zhang, J. G. Mao and F. Kong, *Chin. Chem. Lett.*, 2026, **37**, 110588.
49 X. Y. Li, X. Cheng, C. L. Hu, B. X. Li, Z. Zhou, J. H. Zhang, S. Deng, J. G. Mao and F. Kong, *Angew. Chem., Int. Ed.*, 2025, **64**, e202501481.
50 X. Meng, X. Zhang, Q. Liu, Z. Zhou, X. Jiang, Y. Wang, Z. Lin and M. Xia, *Angew. Chem., Int. Ed.*, 2022, **62**, e202214848.
51 S. Choi and K. M. Ok, *Chem.–Asian J.*, 2025, **20**, e00622.
52 H. Wu, Z. Wei, Z. Hu, J. Wang, Y. Wu and H. Yu, *Angew. Chem., Int. Ed.*, 2024, **63**, e202406318.
53 (*a*) CCDC 2474438: Experimental Crystal Structure Determination, 2026, DOI: 10.5517/ccdc.csd.cc2p1vl6; (*b*) CCDC 2474439: Experimental Crystal Structure Determination, 2026, DOI: 10.5517/ccdc.csd.cc2p1vm7.